

Analysis of the impact of long-term changes in the geomagnetic field on the spatial pattern of the Weddell Sea Anomaly

Ewa Slominska¹, Marek Strumik², Jan Slominski², Roger Haagmans³, Rune
Floberghagen⁴

¹OBSEE, Niska 18/32, 01-034, Warsaw, POLAND

²Space Research Center PAS, Bartycka 18A, 00-716, Warsaw, POLAND

³ESA ESTEC, Keplerlaan 1, 2201 AZ Noordwijk, Netherlands

⁴ESA ESAC, Camino Bajo del Castillo, Urb. Villafranca del Castillo, 28692 Villanueva de la Canada,

Madrid, Spain

Key Points:

- The impact of the geomagnetic field secular variation on the spatial morphology of the Weddell Sea Anomaly (WSA)
- Numerical reconstruction of the WSA derived with the TIEGCM model
- Tracking maximum of the WSA with LEO satellite missions

Abstract

We simulated the impact of long-term changes in the geomagnetic field on the spatial pattern of the Weddell Sea Anomaly (WSA). The Weddell Sea Anomaly, belonging to the region near the tip of the Antarctic Peninsula, Falklands and surrounding seas, is the best-known example of ionospheric reversed diurnal cycle. This paper investigates whether and to what extent long-term changes in the geomagnetic field influence spatial morphology of the WSA. The major concept centers on a normalized density difference index, serving as a measure of difference between dayside and nightside ionospheric density. Through combined analysis of in-situ ionospheric electron density data from past mission CHAMP, on-going ESA mission Swarm and simulations based on the NCAR TIEGCM model, we examine changes in the spatial pattern of the WSA-like anomalies, which could be linked to long-term changes in the geomagnetic field. A series of simulations provides theoretical analysis of changes in the morphology of the WSA on time scales longer than several decades. Numerical analysis shows that from the time when the WSA was discovered (around 1960) till present, maximum of the WSA has migrated by 7 degree in longitude towards the Pacific Ocean, showing clear westward drift, consistent with temporal evolution of the geomagnetic dipole component.

1 Introduction

Reversed ionization diurnal cycle is one of the distinctive features of the Earth's ionospheric F region, which can be briefly characterized by higher values of the peak electron concentration, $N_m F2$, observed in the post-sunset hours rather than around local noon. From the historical perspective, the first evidence of such behavior was found in the ionosphere of the Southern Hemisphere, close to the Antarctic Peninsula and surrounding seas. Bellchambers and Piggott (1958) and Penndorf (1965) commenced to call this specific behavior of the ionosphere, as the Weddell Sea Anomaly (WSA). Further studies, utilizing ground-based data and augmented by increasing number of satellite observations, showed that also in the Northern Hemisphere similar behavior of the ionosphere is registered. In the North, main area of interest concentrates on the Russian sector with Kamchatka, the Bering Sea and the Sea of Okhotsk as focal points. In the literature, we can find also references to the Yakutsk Anomaly (Klimenko et al. (2015)) or "the siberian effect" (Eyfrig (1963)).

Initially, the occurrence of the anomaly was assigned to summertime conditions; thus the phenomenon got broader name as the mid-latitude nighttime summer anomaly (MNSA, Thampi et al. (2009, 2011)). In consequence, numerous papers devoted to the problem of the WSA or MNSA focus on June and December solstices. Nevertheless, there are proofs that this type of ionospheric behavior remains still strong during both equinoxes. This is confirmed in climatological studies exploiting the total electron content (TEC) registrations from TOPEX/JASON-1 (Jee et al. (2009)), in analysis of ionospheric plasma parameters (N_i , $T_{e,i}$, plasma drifts and fluxes) derived from the DMSP data set (Horvath and Lovell (2010)), or by Zhang et al. (2013) who examined the TIMED/GUVI data with interest in occurrence of midlatitude arcs. The term midlatitude arcs refers to enhancements in the electron density in nightside ionosphere, spatially spread across magnetic latitudes of 20° - 40° . Using in-situ electron density registrations from the CNES mission DEMETER, Slominska et al. (2014) showed that above the altitude of 600 kilometers, nighttime plasma density enhancements are an inherent ionospheric attribute, which exhibits modifications in strength and spatial extent due to seasonal variations of the ionosphere.

While the existence of the WSA-like phenomena is undoubted, mechanisms responsible for their appearance are being discussed. Most often, the occurrence of the WSA-like phenomena is attributed to the role of neutral winds (Richards et al. (2017); Lomidze et al. (2016), and references therein) and the morphology of the Earth's magnetic field (the role of declination and inclination) in the regions where anomalous behavior occurs (Horvath and Essex (2003)). While ionospheric ionization is mainly determined by solar radiation, transport of ionospheric plasma is tightly organized by the geometry of the magnetic field, which has an impact on thermospheric winds, generated electric fields, and system of ionospheric currents. The magnetic field structure, which organizes the ionospheric dynamics, is mentioned as a possible cause of some of the regional and global peculiarities in the ionospheric electron density. Horvath and Lovell (2009) stressed out the crucial role of the thermospheric neutral winds in the development of the WSA, by analyzing vertical plasma flows around the WSA site. Thanks to neutral winds, plasma accumulated at lower layers of the ionosphere can be elevated to upper altitudes (Rishbeth (1998), Jee et al. (2005)). Furthermore, confronting the role of neutral winds and vertical $E \times B$ drift, Cnossen and Richmond (2008); Chen et al. (2011) showed that equa-

forward neutral winds dominate the plasma transport and are more fundamental for formation of the WSA in comparison with the ion drift.

In a quantitative analysis focused on the WSA, Richards et al. (2017) (and references therein) reviews previous works and states that widely used interpretation that the WSA results from effects of the geomagnetic declination and inclination on the neutral wind, is insufficient to cause longitudinal variation of the ionospheric electron concentration. Additionally, Richards et al. (2017) questions the concept that downward flux of plasmaspheric plasma is needed for the maintenance of nighttime density enhancements and points out that no additional sources are required. According to an interpretation adopted by the authors, the WSA develops from longitudinally organized distribution of the neutral winds and neutral densities. Furthermore, as noted by Richards et al. (2017), these longitudinal variations occur because the proximity to the auroral zone is not equal along latitudinal direction.

Nevertheless, the role of the Earth's magnetic field cannot be neglected. Direct relation linking components of neutral wind and the geomagnetic field parameters (inclination I and declination D), was discussed by Titheridge (1995) and Rishbeth (1998). To describe the effective neutral wind that trails the plasma along the magnetic field, we need to map both components, meridional (W_M) and zonal (W_Z), on magnetic field lines. This is obtained through the following formula:

$$V_{eff} = 0.5 \cdot \sin 2I \cdot (W_M \cos D \mp W_Z \sin D). \quad (1)$$

Depending on the hemisphere under consideration, "-" is used for the North, while "+" for the South. Diurnal variations of the neutral winds are observed: pre-dawn zonal winds are primarily westward, while post-sunset – mainly eastward. Also, meridional winds change their direction from daytime poleward to nighttime equatorward (Titheridge, 1995). The daytime poleward wind can be expected to transport the plasma to lower altitudes, where the recombination rate is larger, resulting in smaller plasma density in the dayside region. The equatorward nighttime wind acts in the opposite direction, elevating the plasma to higher altitudes and effectively retaining a relatively high density of plasma in the nightside region.

Previous studies of the WSA-like phenomena have been mainly focused on possibly accurate representation of factors contributing to the formation of the WSA (Horvath and Essex (2003); Horvath (2006); Horvath and Lovell (2009); Horvath and Lovell (2010);

Ren et al. (2012); Richards et al. (2017)), as well as has examined the impact of changing solar activity (Jee et al. (2009); Slominska et al. (2014)). Chen et al. (2011) and Thampi et al. (2011) employed dipole field approximation for successful reconstruction of the WSA and MNSA, however, the contribution of secular variation in the Earth's magnetic field has been excluded from the discussion. It is worth to stress out that, on time scales longer than decades, changes in the magnetic field may introduce changes in V_{eff} and in consequence, could affect the spatial distribution of the WSA-like phenomena.

As indicated by Rishbeth (1997), the secular variation leads to a gradual shift in the location of the magnetic poles and the equator, which prompts the migration of the electrojet as well as the deformation of equatorial ionospheric structures. As indicated by Rishbeth (1997), a gradual shift in the location of the magnetic poles and the equator is the strong evidence of the secular variation. In turn, it is expected to observe the migration of the electrojet and possible deformation of equatorial ionospheric structures. On scales of decades, developing variations in inclination and declination can be expected to cause a detectable effect on the structure of the $F2$ -layer, especially in those areas where the influence of winds is remarkably strong due to the morphology of the geomagnetic field. The Atlantic Ocean sector is considered as the region with the most evident signs of the geomagnetic secular variation (Finlay et al. (2016)). Although not in the context of the WSA, Cnossen and Richmond (2008) confirmed findings obtained Rishbeth (1997) and showed that in the time frame of 50 years, changes in the global distribution of the horizontal neutral wind, are mainly in charge of fluctuations of the maximum height and peak concentration of the $F2$ -layer. The authors emphasize a significant role of changes in the declination and the inclination as related to the $\sin(2I)$ term. In addition, taking into account that the Earth's magnetic field dipole moment has decreased by nearly 30% over the past two millenniums, in which almost 9% took place since 1840, modelers speculate (Olson and Amit (2006)) that the ongoing episode of the dipole-moment downtrend can be considered as an indication of a geomagnetic polarity reversal. During the reversal, which may last for several centuries, the dipole field maintains at a diminished level, while the residual field may form an unusual shape, leading to perplexing structures in the ionosphere (Rishbeth (1997)).

Performing extensive analysis of the global representation of TEC data from the TOPEX mission, Horvath and Essex (2003), brought back the interest in the phenomenon of the WSA in the current century. The authors pointed out that due to the vast extent

of the anomaly, its central part lay west of the Faraday ionosonde station over the Bellingshausen Sea instead of the Weddell Sea, and proposed that the more appropriate name should be the Bellingshausen Sea Anomaly. Although the name of the phenomenon has not been changed, this finding suggested an inquiry about the possible migration of this large-scale ionospheric feature.

The aim of this paper is to quantify how and to what extent, changing magnetic field impacts the formation of the WSA. On the other hand, we need to keep in mind, that ionospheric changes purely related to the magnetic field secular variation are small, when compared with typical diurnal, seasonal, solar and magnetic activity related variations of the ionosphere. A combination of measurements of in-situ electron density, from two satellite missions, on-going mission Swarm and past mission CHAMP, provides insight into overall changes in the spatial distribution of the WSA-like phenomena, registered by the two missions. The time frame covered by these two missions is roughly 15 years, which in terms of analysis of secular variation represents a rather scanty data set. Therefore the discussion of the role of the Earth's magnetic field and interpretation of observed trends demands additional analysis employing a physics-based ionospheric model. The NCAR TIEGCM (Thermosphere-Ionosphere-Electrodynamics General Circulation Model) model is selected as a state-of-the-art model suitable for the study. TIEGCM is a time-dependent model, which solves the three-dimensional momentum, continuity and energy conservation equations for neutral and ion species in three spatial dimensions (Richmond et al. (1992)). The International Geomagnetic Reference Field (IGRF - 12th generation, Thébault et al. (2015)) model is implemented in TIEGCM to represent the Earth's main field and its secular variation. It is worth to mention, that the latest set of Gauss coefficients, $g_{n,m}$, and $h_{n,m}$ provided by IGRF, includes high-quality satellite measurements of the magnetic field collected by the Swarm mission.

Presented analysis is divided into 4 sections. Section 2 provides description of the proposed methodology based on the normalized density difference index I_{NDD} . Then in section 3 we introduce satellite data used for the study, as well as describe scenarios examined in the numerical-modeling. Comparison between results from satellite data and numerical modeling is provided in section 4 and discussed in section 5. Section 6 sums up the analysis.

2 Methodology - Normalized density difference index - I_{NDD}

For detection of the WSA-like phenomena, Slominska et al. (2014) examined the concept of the normalized density difference index (I_{NDD}), defined as follows:

$$I_{NDD}(\lambda, \theta) = \frac{N_e^{night}(\lambda, \theta) - N_e^{day}(\lambda, \theta)}{N_e^{night}(\lambda, \theta) + N_e^{day}(\lambda, \theta)} \quad (2)$$

Satellite registrations of in-situ electron density acquired in a local time frame (LT) at the altitude determined by the satellite's orbit are binned into a grid. For each grid node with coordinates, λ as geographic longitude and θ as geographic latitude, N_e^{night} and N_e^{day} denote median electron density measured on ascending and descending passes respectively, separated by 12 hours resulting from the satellite's quasi Sun-synchronous circular orbit. Based on observations of ionospheric plasma density registered by the CNES mission DEMETER, taken at two local times (22:15 - nighttime and 10:15 - daytime), the authors obtained global representation of regions in which ionosphere can be characterized by the reversed diurnal cycle. Under regular conditions (daytime N_e subtracted from nighttime N_e), the index is negative and represents typical ionospheric behavior. If I_{NDD} is greater than 0, it serves as an indicator of the reversed diurnal cycle and manifests possible nighttime enhancements. I_{NDD} is a sort of metric that quantifies a contrast between two ionospheric states separated by 12 hours, thus intervals when the I_{NDD} function peaks exhibit the highest contrast and preferable conditions for NPDEs detection. Since I_{NDD} is normalized, it has a well-defined range of changes from -1 to 1, making it a versatile parameter for comparison between independent data sources and models. Additionally, I_{NDD} operates on relative values instead of absolute measures, which minimize discrepancies originating from instrumental settings, but also provides the capability to track certain trends and patterns in ionospheric behavior. By means of I_{NDD} , we aim to quantify whether long-term changes in the Earth's main magnetic field impact the spatial morphology of the WSA-like phenomena.

3 Data and model

3.1 Satellite data - Swarm and CHAMP

The analysis utilizes in-situ satellite data of ionospheric electron density, measured by the Langmuir probe, onboard the Swarm constellation and the single-satellite mission CHAMP. The study exploits global maps of the I_{NDD} index, which are composed

of monthly sets of data, that are binned into a grid with spatial resolution $10^\circ \times 1^\circ$ in longitudinal and latitudinal direction, respectively. One-day running median is used to remove spikes and fluctuations in the electron density readings. Such procedure is performed over available Swarm dataset assigned with processing version v0501. In the same manner we process the CHAMP dataset.

Swarm mission allows to simultaneously measure plasma properties at two separate altitudes, with three satellites (Alpha (SwA), Bravo (SwB) and Charlie (SwC)) placed in two different polar orbits. Since completion of the orbit acquisition phase in April 2014, one satellite (SwB) is flying in a higher orbit with an inclination of 87.8° and an altitude decreasing from 520 km. The lower pair of satellites, SwA (trailing) and SwC (leading), was placed at an initial altitude of 473 km, an inclination of 87.4° and an ascending node difference of 1.4° . The CHAMP's orbit was lower than the pair from the Swarm constellation, with almost circular, near-polar orbit and slow precession. The launch of CHAMP took place in July 2000. CHAMP was placed into a near-polar orbit with an inclination of 87° and its initial altitude was 454 km. The mission lasted 10 years, and in its final stage the orbit was decayed to about 250 km. Unlike DEMETER, Swarm and CHAMP provide full local time coverage, but Swarm A/C, Swarm B, and CHAMP have different LT precession rates. For the two lower satellites, Swarm A/C, it takes 265 days to cover 24 hours of LT (for an individual node of the orbit), and for the higher-orbit spacecraft, Swarm B, it is 280 days. In case of CHAMP, 24 hours of LT are covered in approximately 260 days. Taking into account that the drift of LT is roughly 3 hours per month, for each monthly set, we extract LT of the middle day of the month as representing mean LT. The following pairs of monthly sets from CHAMP and Swarm A/C meet selection criteria of seasonal consistency and LTs suitable for observations of NPDEs (± 2 hours around local midnight/noon):

- March case: CHAMP 2009 (alt. 325 km), Swarm Alpha 2016 (alt. 455 km) (LT:2200-2300)
- December case: CHAMP 2004 (alt. 376 km), Swarm Alpha 2016 (alt. 451 km) (LT:2200)
- August case: CHAMP 2005 (alt. 363 km), Swarm Alpha 2018 (alt. 446 km) (LT:0000-0100)

While DEMETER-based analysis was oriented on the single pair of local times, Swarm and CHAMP provide capability to expand this analysis. Additionally, extended LT coverage allows to provide reconstruction of the index in the universal time (UT) frame, and proves that the WSA is the strongest example of the diurnal reversed cycle. Since this part of analysis is out of scope of the current paper, we only refer the reader to the animation provided in the supporting material.

3.2 TIEGCM simulations

In-situ measurements are supplemented with the synthetic index I_{NDD} derived from the TIEGCM model. For the present work, the TIEGCM 2.0 version is used with the double-resolution. Such configuration provides a grid of $2.5^\circ \times 2.5^\circ$ for latitude and longitude, and 58 pressure levels in the vertical direction. The lower boundary of the model is at approximately 97 km, and the upper boundary ranges from 400 to 700 km depending on the solar activity and settings of solar flux. The option for lower boundary forcing is switched off to minimize the contribution from factors other than the magnetic field. The purpose of using TIEGCM is to reconstruct the I_{NDD} index at the altitude of a satellite, thus we make an approximation between neighboring pressure levels in order to obtain the optimal agreement for the scale height.

Focusing on the role of the Earth's magnetic field and its impact on the formation of the WSA-like phenomena, we examine independent scenarios for the TIEGCM runs:

- Scenario #1: TIEGCM runs with a realistic magnetic field configuration determined by the IGRF model for a set of selected years.
- Scenario #2: Simplified magnetic field model reduced to dipole representation, with various configurations reflecting different eccentricity and tilt angle of the magnetic dipole.

Through all simulations, we used identical configuration of controlling parameters describing solar minimum and quiet geomagnetic conditions. The following parameters were used in the TIEGCM standalone runs: the solar flux ($F107 = 70$), the cross-tail potential ($CTPOTEN = 30$) and the hemispheric power ($POWER = 18$).

The model web-page (<http://www.hao.ucar.edu/modeling/tgcm/tiegcm2.0/userguide/html/>) provides more details on the physical meaning of the parameters used

in the configuration and physics included in the model. Such configuration of model runs, minimizes the variability of the index originating from varying solar conditions and allows to isolate effects related to changes in the main magnetic field. Before the index is computed, the TIEGCM output for the diagnostic field of the electron density N_e is converted to the LT frame. Using configurations defined above, we perform 5-day standalone runs, with the time-resolution of 10 minutes for March equinox, at two separate altitudes 360 km (corresponding to the CHAMP's orbit), and 460 km (as an equivalent of the Swarm's A/C orbit). Simulations are carried out for the years 1910, 1960, 1980, 2005, and 2015.

4 Results

4.1 Recognition of NPDEs

Figure 1 presents results of monthly maps of I_{NDD} based on the satellite data from CHAMP (left column) and Swarm (right column) meeting the selection criteria defined in section 3.1. Global representation of the TIEGCM-based index is gathered in Figure 2. The numerical-modeling results are provided at two altitude levels, 360 (left column in Figure 2) and 460 (right column in Figure 2) kilometers for midnight/noon conditions.

In order to facilitate recognition of the WSA and NPDEs and their evolution, we apply red-toned color coding to regions for which the I_{NDD} index obtains values greater than 0. Remaining areas, which show typical ionospheric behavior are marked only with blueish isolines. The same method for data visualization is applied to model- and data-derived index, but note the difference in color scales. The TIEGCM-derived index has smaller amplitude hence the scale is reduced to the range from -0.5 to 0.5. To simplify notation, throughout the text, we use one LT, but by referring to I_{NDD} at 00:00 LT, we keep in mind that the index is computed using the difference in electron densities between midnight and noon, and the same applies to every other hour.

In general, the spatial pattern of NPDEs derived with the CHAMP and Swarm data (Figure 1) as well as the TIEGCM model (see Figure 2), confirms findings from previous studies and indicates that in the Southern Hemisphere, region from the southern half of South America through Antarctic Peninsula and neighboring archipelagos and seas, the Weddell Sea and the Bellingshausen Sea and finally coasts of Antarctica, is the paramount sector for observations of reversed diurnal cycle. Corresponding effect in the Northern Hemisphere is localized in two spots, first one, in the central part of the Atlantic Ocean

expanding towards the Southern Europe (for convenience we name it Northern Atlantic Enhancement - NAE) and the second one lays between the Kamchatka Peninsula, the Sea of Okhotsk and Japan (in brief Okhotsk Sea Enhancements - OSE). In general, model- and data-derived maps of the index, show that northern hemispheric enhancements are weaker than the southern one and they tend to exhibit much stronger dependence on the altitude. According to numerical results, at 460 km only NAE emerges in 2005 and strengthens further on, but with no evidence of OSE. In contrast NAE intensifies and forms a structure slowly progressing from the continental Europe towards the east coast of Northern America. It is quite remarkable, that the Swarm and CHAMP data show that OSE does not occur simultaneously in all analyzed cases, giving evidence that in the North reversed ionospheric cycle is more dependent on altitude, LTs and seasons.

Comparing two analyzed missions, we note more extended spatial coverage of NPDEs for Swarm than for CHAMP, which in particular is manifested by prolonged midlatitude (between 20-40° of latitude) bands of enhanced electron densities clearly marked in the hemisphere of local winter (in the North for December case (Figure 1c,d) and in the South for August case (Figure 1e,f) in Swarm data). Different orbital altitudes of these two missions possibly contribute to the observed patterns of I_{NDD} . Even though altitudinal differences are relatively small, for the March comparison (Figure 1a,b) the difference in altitude is greater than 100 km, and in remaining instances is around 80 km, it is quite essential to note that CHAMP's orbit nearly cuts through the maximum of the $F2$ peak, while Swarm is slightly above. Zakharenkova et al. (2017) showed, that the most-pronounced WSA effect, as a maximal electron density exceed over the noon-time values, corresponds to altitudes above 400 - 500 km, which justifies stronger effects registered by Swarm.

4.2 Tracking maximum of the WSA

Long-term changes of the WSA are the scope of the study, and expected effect related to secular variation of the geomagnetic field would be in the form of a shift in position of the central part of the anomaly. A closer look at the longitude sector between 0° meridian and 60°W meridian in the numerical simulations (Figure 2), shows that throughout examined years, the eastern boundary of the WSA significantly shrinks and approaches 60°W meridian, while its western edge vaguely passes through 120°W. In terms of the magnitude of the WSA, noticeable reduction is found. In order to gauge the impact of

geomagnetic secular variation, we search for a maximum of the WSA in terms of the index and we track its location. Analysis is performed in the southern sector of the Western Hemisphere (third quadrant of the map).

Satellite-derived maps of the index, capture seasonal and LT-related variations, which in overall are manifested by large fluctuations of the amplitude, as well as shifts along the latitude. Based on the index maxima gathered in Table 1, in terms of absolute values, it looks like measurements from Swarm are considerably more stable. All these variations have major impact on the behavior of the index and are observed as rather quickly varying effects, that may conceal subtle contribution related to the magnetic field. Thus, considering the time frame covered by the CHAMP and Swarm missions, we provide averaged estimation of the WSA location for each spacecraft, based on all available data meeting criteria of corresponding LTs, but without distinction between seasons.

To maximize the amount of data for analysis, in the same manner as we construct monthly maps, we take 6-day data sets to generate global maps of the index. Next, we extract maxima of I_{NDD} in the third quadrant. Finally, we group derived values into bins based on LTs and for every bin compute medians of I_{NDD} . Results obtained from the satellite observations, divided into three LT bins suitable for observations of NPDEs are gathered in Table 2. Projection of gathered results is provided in Figure 3 for the midnight/noon conditions, together with maxima computed for the numerical simulations. Satellite-derived locations are indicated with hexagonal markers, numerical results are denoted with diamonds and stars, depending on the altitude.

Focusing on both missions, we see that averaged maximum of the WSA derived for each satellite from the Swarm mission is relocated west along the longitude by at least 10° , towards the Pacific Ocean, when compared with maximum from CHAMP. Latitudinal shift is less obvious, while for 00/12 and 02/14 LTs CHAMP's maxima are displaced toward high latitude, opposite effect is found for the pre-midnight conditions. For the relatively short interval, spanning over the CHAMP and Swarm missions, between years 2005 and 2015, numerical simulations do not exhibit the drifting of the WSA, though a decrease of the amplitude of the index for examined LT bins and both altitudes is reported (see Table 3). However, on time scales longer than several decades (from 1910 to 2015) substantial westward migration of the WSA is observed in the numerical simulations. For a specified LT and altitude, maximum of the index relocates in the west-

ward direction towards Pacific, with stronger effect at lower altitude (diamond markers in Figure 3).

The longitudinal shift of 10° derived from the satellite data, seems to be overestimated. This is partly a consequence of the assumption that we averaged out dynamic morphology of I_{NDD} that is strongly organized by several physical drivers (orbital altitudes, solar activity variations and slight shifts in local time) having an implication on observed patterns. Despite contradicting results for the analyzed decade, general trend of migration should not be questioned, and as it is shown in the next section, it is in agreement with general behavior of the geomagnetic field, especially in the Western Hemisphere.

5 Discussion

5.1 Analysis of simplified configurations of dipole-field approximations

Full set of Gauss coefficients of the IGRF-12 model allows to capture long-term changes in the main field, with contribution from dipole and non-dipole terms, and its impact on the spatial changes in the WSA morphology. For ionospheric applications, the dipole field dominates, therefore for an explanation of modeled results, it is sufficient to focus mainly on secular variations of the dipole component. First eight Gauss coefficients define an eccentric dipole, displaced and tilted with respect to the Earth's rotation axis, while the first three Gauss coefficients represent contributions to a centered tilted dipole (Chapman and Bartels (1962), Fraser-Smith (1987)). Conducting a simplified experiment using the TIEGCM model we aim to show that changes in the tilt angle and eccentricity of the magnetic dipole have a profound influence on the spatial morphology of the WSA.

As a starting point, we take an eccentric dipole (see Figure 4a) with the tilt angle of 11 degrees, positioned about 400 km from the center of the Earth (specified by eight Gauss coefficients). In the next run, we reduce the eccentricity by placing the tilted geomagnetic dipole in the Earth's center (see Figure 4b). Results for spatial distribution of I_{NDD} for those two cases around midnight/noon (0000LT) exhibit apparent signatures of the WSA manifested as patches of positive values of I_{NDD} located in the Southern Hemisphere and spanning over the longitude sector between 120°W - 45°W . Reduction of the offset between the geomagnetic dipole and the Earth's rotation axis lessens inter-hemispheric asymmetry in the magnetic field and in consequence leads to more uniform

distribution of the electron density and the index. In such configuration, not only the area of the WSA is reduced, but also northern hemispheric enhancements spanning over parts of the Eastern Europe (longitude sectors between 15°E-45°E) vanish. The third run formulates speculative and exaggerated scenario to the previous case where the orientation of the geomagnetic tilted dipole is opposite with respect to the Earth's rotation axis. In such configuration, the WSA occurs in the Indian Ocean sector, while all other typical ionospheric features (dip equator, location of auroral ovals) exhibit typical mirrored reflection (see Figure 4c). In the final run, the tilt angle is set to 0 (axial dipole), which in consequence eliminates the WSA. Under such conditions, there is full symmetry between both hemispheres and ionospheric structure is homogenous, practically symmetric across latitudes regarding the straightened dip equator (see Figure 4d). Ionization controlled by the solar zenith angle plays the major role and in consequence, for near midnight conditions, we observe nearly longitudinally uniform distribution of negative values of I_{NDD} .

5.2 Westward drift of the WSA

Bearing in mind the results of numerical experiments with simplified configurations from the preceding subsection, we take a closer look at the secular variation of the dipole component. Following formalism provided by Chapman and Bartels (1962) and updated by Fraser-Smith (1987); Koochak and Fraser-Smith (2017) we compute the properties of the eccentric dipole, using the first eight Gauss coefficients. This allows us to reconstruct time series of the dipole tilt angle and compute the total displacement of the geomagnetic dipole from the center of the Earth.

Figure 3 shows the variation of the eccentric dipole position projected on the Earth's surface with respect to the equatorial plane. Applied color scale, reflects the tilt angle. Results indicate a systematic reduction in the tilt angle (from purple through reds towards green), with a rapid decrease which commenced around 1960. As shown by Amit and Olson (2008), the declining trend in the dipole tilt is first and foremost caused by changes in the equatorial component of the dipole moment. Currently decreasing tendency is observed for the equatorial and the axial component of the dipole moment, as well as the dipole tilt angle and the total intensity of the dipole moment. From Figure 3, we note that geomagnetic dipole steadily moves away from the equatorial plane and the Earth's center. Koochak and Fraser-Smith (2017) estimated a rate of migration at

the level of 2.5 kilometers per year, showing that at the current stage the relocation reaches 9% of the Earth's radius with nearly 580 km, while in 1980 it was around 488.6 km.

As shown in previous studies (Siscoe and Christopher (1975); Cnossen and Richmond (2012)) and in simplified simulations presented in the current paper, the dipole tilt angle determines the geographical location of the geomagnetic pole and polar cap boundaries. The strength of the Joule heating, the structure of ionospheric convection patterns and the spatial distribution of energetic particle precipitation is also organized by the dipole tilt angle. Variations in the Joule heating with tilt angle lead to changes in temperature and neutral winds and in consequence impact thermospheric composition. Modulations in the O/N_2 ratio change electron-ion recombination rates, and lead to variations in the $F2$ electron density.

On the one hand, decreasing dipole tilt angle implies that the WSA's expansion towards the low latitude regions as well as its longitudinal variation may be minimized. On the other hand, the second principal secular variation of the dipole field, the westward drift, also affects morphology of the WSA. The dipole part is moving away from the Earth's center, with the movement accompanied by steady northward migration above the equatorial plane (see Figure 3, position of the geomagnetic dipole projected on the Earth's surface). Stronger eccentricity of the dipole component may lead to much more pronounced asymmetries between two hemispheres, excessive longitudinal variations, and strengthening of the WSA across the Pacific Ocean, westward from the Antarctic Peninsula. Such behavior is consistent with the modeled pattern of the WSA migration, but also similar tendency seems to emerge from a comparison of selected Swarm and CHAMP maxima of I_{NDD} for specified LTs.

The proximity of the Weddell Sea Anomaly to the region of the South Atlantic Anomaly (SAA), suggests that the impact of geomagnetic secular variation may be visible in the same way as it is observed for the SAA. Significant evidence of the westward migration of the Earth's magnetic field is documented by secular variation of the SAA. Numerous studies (Jones et al. (2017); Pavón-Carrasco and Santis (2016) and references therein) confirm that the total intensity of the magnetic field is changing. Strong expansion of the South Atlantic Anomaly towards continental regions of South America is recorded, with the minimum of the magnetic field intensity located in Brazil.

Although, the WSA as the most prominent example of NPDEs is the focal point of the study, to sum up conducted work, we provide quantitative evaluation of long-term changes in simulated I_{NDD} on a global scale. The measure is expressed through percentage difference δI_{NDD} between selected epochs (2015 and 1910) with respect to the maximum value of the I_{NDD} index for a given LT bin and altitude in 2015. Estimation is made for a given altitude and local times (see Figure 5). In most regions, at mid- and high latitudes, modifications, both positive and negative, are rather small and do not go beyond 15% (in Figure 5 areas marked with pale grey and pale salmon tones). However 4 separate spots emerge as areas of intensified changes of I_{NDD} , including the region of the Weddell Sea. Comparison for examined time intervals, indicates that the strength of the anomaly diminishes steadily in the Weddell Sea region (red tones denote negative tendency) and builds up on the western side of the Antarctic Peninsula in the Bellingshausen Sea and across the Pacific Ocean, giving evidence of general westward drift of this particular ionospheric feature. The most intense variations in spatial morphology of I_{NDD} are expected to occur in the longitude sector of the Atlantic Ocean, on both sides of the geomagnetic dip equator. It suggests that for examined March equinox conditions, nighttime enhancements in the Atlantic region are stronger than those in the Siberian region. Obtained global pattern of changes in the morphology of I_{NDD} is in agreement with results from comprehensive studies by Cnossen and Richmond (2008, 2013), who concluded that in comparison to other parts of the world, in the Atlantic region, defined as the area between 40°S - 40°N and 100° W - 50° E, secular variation of the Earth's magnetic field are in charge of most ionospheric trends. Observed significant variations of magnetic field inclination dominate the overall behavior, having an impact on the vertical component of plasma transport. In terms of changes in Sq amplitude, Cnossen and Richmond (2013) recognized significant regional dependency, associated with already mentioned relocation of the dip equator and the westward drift of the geomagnetic field. It is worth to stress out, that modulations of the field intensity were not considered as fundamental for derived patterns of ionospheric parameters.

The strength of the Earth's magnetic field changes over time. Long-term changes in the magnetic field reveal decreasing tendency of the intensity of the main dipole component (see the second column in Table 3), which has an effect on ionospheric conductivity (expressed through the Pedersen and Hall conductivities). As shown by Takeda (1996) when the field strength decreases, altitudes of Pedersen conductivity maxima shift

upward, and height-integrated Pedersen and Hall conductivities are enhanced. Although conductivity is proportional to the concentration of the electron and ions, and inversely proportional to the magnetic field intensity, we find a gradual decrease in the amplitude of I_{NDD} . Table 3 summarizes performed simulations, grouping maxima of the index with locations for analyzed LT bins and altitudes. Knowing that all simulations are performed at a fixed level of solar activity and identical seasons, we can exclude these factors as a plausible cause of the observed trend. Since I_{NDD} operates on the relative difference between dayside and nightside ionosphere, the relation between the index and changes in magnetic field intensity is not straightforward, and more complex dependencies take place. This finding awaits further verification with in-situ measurements, however, at the current stage of the Swarm mission we still lack sufficient representation of data.

6 Conclusions

In this article, we have made an attempt to investigate the relationship between long-term changes in the magnetic field and spatial morphology of the WSA. To our knowledge, no dedicated study of this aspect has been conducted. The presented analysis joins the advanced ionospheric model and in-situ measurements derived from two satellite missions. Utilizing the I_{NDD} index, we have tracked the location of the maximum of the anomaly. Modeled results indicate that:

- from the time when the WSA was discovered (around 1960) to the present time, the central part of the anomaly migrated by 7 degree in longitude westward;
- drift in latitude is less obvious and depends on considered local time, as well as the altitude.

Confrontation of results from numerical modeling with measurements from two satellite missions, Swarm and CHAMP, confirms a slight shift in the WSA location towards western parts of the Pacific Ocean, however obtained absolute values of displacement suggest to be overestimated. Obtained result prove that is essential to acquire possibly long representation of measurements from one satellite mission (at least 10 or 15 years of data) in order to conduct this type of analysis for more trustworthy outcome with additional interest on thorough investigation of a complete solar cycle.

Through a series of simplified numerical experiments we aimed to investigate how varying configurations of the geomagnetic field affect the WSA phenomenon, and prove

that the structure and configuration of the geomagnetic field is crucial for the spatial pattern of the WSA. The WSA region was the focal point of the study, but it is worth to mention that the central sector of the Atlantic Ocean is characterized by more intense changes in the magnetic field configuration. A glimpse of results indicates that the occurrence of NAE exhibits prominent variations, which are of interest for further studies. In particular, the constellation of Swarm satellites should provide more detailed image of changes in the spatial morphology of NPDEs on a global scale simultaneously at two altitudinal levels.

Acknowledgment

- This work was supported by the European Space Agency, in the framework of ESA Contract No. 4000112769/14/NL/FF/gp.
- L3 Swarm I_{NDD} product is available on regular basis from the following address: <http://swarm4anom.cbk.waw.pl/s4a/prod.html>.
- Swarm LP L1 data were obtained from the ESA dissemination servers freely accessible to all users via anonymous access. <ftp://swarm-diss.eo.esa.int>.
- Authors would like to thank the NCAR TIEGCM Team, for making the source code of the model available to the public.
- CHAMP Langmuir Probe data were obtained from the CHAMP ISDC Data Base provided by GFZ Potsdam ftp servers.

References

- Amit, H., & Olson, P. (2008, February). Geomagnetic dipole tilt changes induced by core flow. *Physics of the Earth and Planetary Interiors*, 166(3-4), 226–238. Retrieved from <https://doi.org/10.1016/j.pepi.2008.01.007> doi: 10.1016/j.pepi.2008.01.007
- Bellchambers, W. H., & Piggott, W. R. (1958, December). Ionospheric measurements made at halley bay. *Nature*, 182(4649), 1596–1597. Retrieved from <https://doi.org/10.1038/1821596a0> doi: 10.1038/1821596a0
- Chapman, S., & Bartels, J. (1962). *Geomagnetism* (No. v. 1). Clarendon Press. Retrieved from <https://books.google.pl/books?id=W5AJAQAIAAJ>
- Chen, C. H., Huba, J. D., Saito, A., Lin, C. H., & Liu, J. Y. (2011, apr). Theoretical study of the ionospheric weddell sea anomaly using SAMI2. *Journal of Geo-*

- 548 *physical Research: Space Physics*, 116(A4), n/a–n/a. Retrieved from [https://](https://doi.org/10.1029/2010ja015573)
549 doi.org/10.1029/2010ja015573 doi: 10.1029/2010ja015573
- 550 Cnossen, I., & Richmond, A. D. (2008, August). Modelling the effects of changes
551 in the earth's magnetic field from 1957 to 1997 on the ionospheric hmf2 and
552 fof2 parameters. *Journal of Atmospheric and Solar-Terrestrial Physics*, 70,
553 1512-1524. doi: 10.1016/j.jastp.2008.05.003
- 554 Cnossen, I., & Richmond, A. D. (2012). How changes in the tilt angle of the ge-
555 omagnetic dipole affect the coupled magnetosphere-ionosphere-thermosphere
556 system. *Journal of Geophysical Research: Space Physics*, 117(A10). Retrieved
557 from [https://agupubs.onlinelibrary.wiley.com/doi/abs/10.1029/](https://agupubs.onlinelibrary.wiley.com/doi/abs/10.1029/2012JA018056)
558 [2012JA018056](https://agupubs.onlinelibrary.wiley.com/doi/abs/10.1029/2012JA018056) doi: 10.1029/2012JA018056
- 559 Cnossen, I., & Richmond, A. D. (2013, February). Changes in the earths magnetic
560 field over the past century: Effects on the ionosphere-thermosphere system
561 and solar quiet (sq) magnetic variation. *Journal of Geophysical Research:*
562 *Space Physics*, 118(2), 849–858. Retrieved from [https://doi.org/10.1029/](https://doi.org/10.1029/2012ja018447)
563 [2012ja018447](https://doi.org/10.1029/2012ja018447) doi: 10.1029/2012ja018447
- 564 Eyfrig, R. W. (1963). The effect of the magnetic declination on the f 2 layer. *Jour-*
565 *nal of Geophysical Research*, 68(9), 2529-2530. Retrieved from [https://](https://agupubs.onlinelibrary.wiley.com/doi/abs/10.1029/JZ068i009p02529)
566 agupubs.onlinelibrary.wiley.com/doi/abs/10.1029/JZ068i009p02529
567 doi: 10.1029/JZ068i009p02529
- 568 Finlay, C. C., Olsen, N., Kotsiaros, S., Gillet, N., & Tøffner-Clausen, L. (2016, July).
569 Recent geomagnetic secular variation from swarm and ground observatories as
570 estimated in the CHAOS-6 geomagnetic field model. *Earth, Planets and Space*,
571 68(1). Retrieved from <https://doi.org/10.1186/s40623-016-0486-1> doi:
572 10.1186/s40623-016-0486-1
- 573 Fraser-Smith, A. C. (1987). Centered and eccentric geomagnetic dipoles and their
574 poles, 1600–1985. *Reviews of Geophysics*, 25(1), 1. Retrieved from [https://](https://doi.org/10.1029/rg025i001p00001)
575 doi.org/10.1029/rg025i001p00001 doi: 10.1029/rg025i001p00001
- 576 Horvath, I. (2006, December). A total electron content space weather study of
577 the nighttime weddell sea anomaly of 1996/1997 southern summer with
578 TOPEX/poseidon radar altimetry. *Journal of Geophysical Research*,
579 111(A12). Retrieved from <https://doi.org/10.1029/2006ja011679> doi:
580 10.1029/2006ja011679

- 581 Horvath, I., & Essex, E. (2003, April). The weddell sea anomaly observed with
582 the topex satellite data. *Journal of Atmospheric and Solar-Terrestrial Physics*,
583 65(6), 693–706. Retrieved from [https://doi.org/10.1016/s1364-6826\(03\)](https://doi.org/10.1016/s1364-6826(03)00083-x)
584 00083-x doi: 10.1016/s1364-6826(03)00083-x
- 585 Horvath, I., & Lovell, B. C. (2009). Investigating the relationships among the
586 South Atlantic Magnetic Anomaly, southern nighttime midlatitude trough,
587 and nighttime weddell Sea Anomaly during southern summer. *Journal of*
588 *Geophysical Research: Space Physics*, 114(A2), n/a–n/a. Retrieved from
589 <http://dx.doi.org/10.1029/2008JA013719> doi: 10.1029/2008JA013719
- 590 Horvath, I., & Lovell, B. C. (2010, January). Investigating the southern daytime
591 midlatitude trough’s relation with the daytime Weddell Sea Anomaly during
592 equinoxes. *Journal of Geophysical Research (Space Physics)*, 115, 1302. doi:
593 10.1029/2008JA014002
- 594 Jee, G., Burns, A. G., Kim, Y.-H., & Wang, W. (2009). Seasonal and solar ac-
595 tivity variations of the weddell sea anomaly observed in the TOPEX total
596 electron content measurements. *Journal of Geophysical Research: Space*
597 *Physics*, 114(A4), n/a–n/a. Retrieved from [http://dx.doi.org/10.1029/](http://dx.doi.org/10.1029/2008JA013801)
598 2008JA013801 doi: 10.1029/2008JA013801
- 599 Jee, G., Schunk, R. W., & Scherliess, L. (2005, July). On the sensitivity of to-
600 tal electron content (TEC) to upper atmospheric/ionospheric parameters.
601 *Journal of Atmospheric and Solar-Terrestrial Physics*, 67(11), 1040–1052.
602 Retrieved from <https://doi.org/10.1016/j.jastp.2005.04.001> doi:
603 10.1016/j.jastp.2005.04.001
- 604 Jones, A. D., Kanekal, S. G., Baker, D. N., Klecker, B., Looper, M. D., Mazur,
605 J. E., & Schiller, Q. (2017, January). SAMPEX observations of the south
606 atlantic anomaly secular drift during solar cycles 22-24. *Space Weather*, 15(1),
607 44–52. Retrieved from <https://doi.org/10.1002/2016sw001525> doi:
608 10.1002/2016sw001525
- 609 Klimenko, M., Klimenko, V., Karpachev, A., Ratovsky, K., & Stepanov, A. (2015,
610 April). Spatial features of weddell sea and yakutsk anomalies in foF2 di-
611 urnal variations during high solar activity periods: Interkosmos-19 satel-
612 lite and ground-based ionosonde observations, IRI reproduction and GSM
613 TIP model simulation. *Advances in Space Research*, 55(8), 2020–2032.

- 614 Retrieved from <https://doi.org/10.1016/j.asr.2014.12.032> doi:
615 10.1016/j.asr.2014.12.032
- 616 Koochak, Z., & Fraser-Smith, A. C. (2017, oct). An update on the centered and ec-
617 centric geomagnetic dipoles and their poles for the years 1980-2015. *Earth and*
618 *Space Science*, 4(10), 626–636. Retrieved from [https://doi.org/10.1002/](https://doi.org/10.1002/2017ea000280)
619 [2017ea000280](https://doi.org/10.1002/2017ea000280) doi: 10.1002/2017ea000280
- 620 Lomidze, L., Scherliess, L., & Schunk, R. W. (2016, March). Modeling and anal-
621 ysis of ionospheric evening anomalies with a physics-based data assimilation
622 model. *Journal of Atmospheric and Solar-Terrestrial Physics*, 140, 65–78.
623 Retrieved from <https://doi.org/10.1016/j.jastp.2016.02.009> doi:
624 10.1016/j.jastp.2016.02.009
- 625 Olson, P., & Amit, H. (2006, August). Changes in earth’s dipole. *Naturwis-*
626 *senschaften*, 93(11), 519–542. Retrieved from [https://doi.org/10.1007/](https://doi.org/10.1007/s00114-006-0138-6)
627 [s00114-006-0138-6](https://doi.org/10.1007/s00114-006-0138-6) doi: 10.1007/s00114-006-0138-6
- 628 Pavón-Carrasco, F. J., & Santis, A. D. (2016, April). The south atlantic anomaly:
629 The key for a possible geomagnetic reversal. *Frontiers in Earth Science*,
630 4. Retrieved from <https://doi.org/10.3389/feart.2016.00040> doi:
631 10.3389/feart.2016.00040
- 632 Penndorf, R. (1965). The average ionospheric conditions over the Antarctic. In
633 *Geomagnetism and Aeronomy: Studies in the Ionosphere, Geomagnetism and*
634 *Atmospheric Radio Noise* (pp. 1–45). American Geophysical Union. Retrieved
635 from <http://dx.doi.org/10.1029/AR004p0001> doi: 10.1029/AR004p0001
- 636 Ren, Z., Wan, W., Liu, L., Le, H., & He, M. (2012, March). Simulated midlatitude
637 summer nighttime anomaly in realistic geomagnetic fields. *Journal of Geophys-*
638 *ical Research: Space Physics*, 117(A3), n/a–n/a. Retrieved from [https://doi](https://doi.org/10.1029/2011ja017010)
639 [.org/10.1029/2011ja017010](https://doi.org/10.1029/2011ja017010) doi: 10.1029/2011ja017010
- 640 Richards, P. G., Meier, R. R., Chen, S.-P., Drob, D. P., & Dandenault, P. (2017,
641 June). Investigation of the causes of the longitudinal variation of the electron
642 density in the weddell sea anomaly. *Journal of Geophysical Research: Space*
643 *Physics*, 122(6), 6562–6583. Retrieved from [https://doi.org/10.1002/](https://doi.org/10.1002/2016ja023565)
644 [2016ja023565](https://doi.org/10.1002/2016ja023565) doi: 10.1002/2016ja023565
- 645 Richmond, A. D., Ridley, E. C., & Roble, R. G. (1992). A thermosphere/ionosphere
646 general circulation model with coupled electrodynamics. *Geophysical Re-*

- 647 *search Letters*, 19(6), 601–604. Retrieved from [http://dx.doi.org/10.1029/](http://dx.doi.org/10.1029/92GL00401)
648 92GL00401 doi: 10.1029/92GL00401
- 649 Rishbeth, H. (1997, January). Long-term changes in the ionosphere. *Advances*
650 *in Space Research*, 20(11), 2149–2155. Retrieved from [https://doi.org/10](https://doi.org/10.1016/s0273-1177(97)00607-8)
651 .1016/s0273-1177(97)00607-8 doi: 10.1016/s0273-1177(97)00607-8
- 652 Rishbeth, H. (1998, September). How the thermospheric circulation affects the iono-
653 spheric f2-layer. *Journal of Atmospheric and Solar-Terrestrial Physics*, 60(14),
654 1385–1402. Retrieved from [https://doi.org/10.1016/s1364-6826\(98\)00062](https://doi.org/10.1016/s1364-6826(98)00062-5)
655 -5 doi: 10.1016/s1364-6826(98)00062-5
- 656 Siscoe, G. L., & Christopher, L. (1975). Effects of geomagnetic dipole variations on
657 the auroral zone locations. *Journal of geomagnetism and geoelectricity*, 27(6),
658 485–489. Retrieved from <https://doi.org/10.5636/jgg.27.485> doi: 10
659 .5636/jgg.27.485
- 660 Slominska, E., Blecki, J., Lebreton, J.-P., Parrot, M., & Slominski, J. (2014).
661 Seasonal trends of nighttime plasma density enhancements in the topside
662 ionosphere. *Journal of Geophysical Research: Space Physics*, 119(8), 6902–
663 6912. Retrieved from <http://dx.doi.org/10.1002/2014JA020181> doi:
664 10.1002/2014JA020181
- 665 Takeda, M. (1996, April). Effects of the strength of the geomagnetic main
666 field strength on the dynamo action in the ionosphere. *Journal of Geo-*
667 *physical Research: Space Physics*, 101(A4), 7875–7880. Retrieved from
668 <https://doi.org/10.1029/95ja03807> doi: 10.1029/95ja03807
- 669 Thampi, S. V., Balan, N., Lin, C., Liu, H., & Yamamoto, M. (2011, January).
670 Mid-latitude summer nighttime anomaly (MSNA) - observations and model
671 simulations. *Annales Geophysicae*, 29(1), 157–165. Retrieved from [https://](https://doi.org/10.5194/angeo-29-157-2011)
672 doi.org/10.5194/angeo-29-157-2011 doi: 10.5194/angeo-29-157-2011
- 673 Thampi, S. V., Lin, C., Liu, H., & Yamamoto, M. (2009, October). First tomo-
674 graphic observations of the midlatitude summer nighttime anomaly over japan.
675 *Journal of Geophysical Research: Space Physics*, 114(A10). Retrieved from
676 <https://doi.org/10.1029/2009ja014439> doi: 10.1029/2009ja014439
- 677 Thébault, E., Finlay, C. C., Beggan, C. D., Alken, P., Aubert, J., Barrois, O., ...
678 Zvereva, T. (2015, may). International geomagnetic reference field: the
679 12th generation. *Earth, Planets and Space*, 67(1). Retrieved from <https://>

doi.org/10.1186/s40623-015-0228-9 doi: 10.1186/s40623-015-0228-9

Titheridge, J. (1995, December). Winds in the ionosphere—a review. *Journal of Atmospheric and Terrestrial Physics*, 57(14), 1681–1714. Retrieved from [https://doi.org/10.1016/0021-9169\(95\)00091-f](https://doi.org/10.1016/0021-9169(95)00091-f) doi: 10.1016/0021-9169(95)00091-f

Zakharenkova, I., Cherniak, I., & Shagimuratov, I. (2017, August). Observations of the weddell sea anomaly in the ground-based and space-borne TEC measurements. *Journal of Atmospheric and Solar-Terrestrial Physics*, 161, 105–117. Retrieved from <https://doi.org/10.1016/j.jastp.2017.06.014> doi: 10.1016/j.jastp.2017.06.014

Zhang, Y., Paxton, L. J., & Kil, H. (2013). Nightside midlatitude ionospheric arcs: Timed/guvi observations. *Journal of Geophysical Research: Space Physics*, 118(6), 3584–3591. Retrieved from <http://dx.doi.org/10.1002/jgra.50327> doi: 10.1002/jgra.50327

Table 1. Maxima of I_{NDD} for selection of cases presented in Figure 1

Case	Max(I_{NDD}) Swarm	Coordinates	Max(I_{NDD}) CHAMP	Coordinates
March	0.608	95.0°W/ 57.5°S	0.373	85.0°W/ 60.5°S
December	0.673	85.0°W/ 59.5°S	0.728	85.0°W/ 63.5°S
August	0.602	85.0°W/ 53.5°S	0.285	85.0°W/ 56.5°S

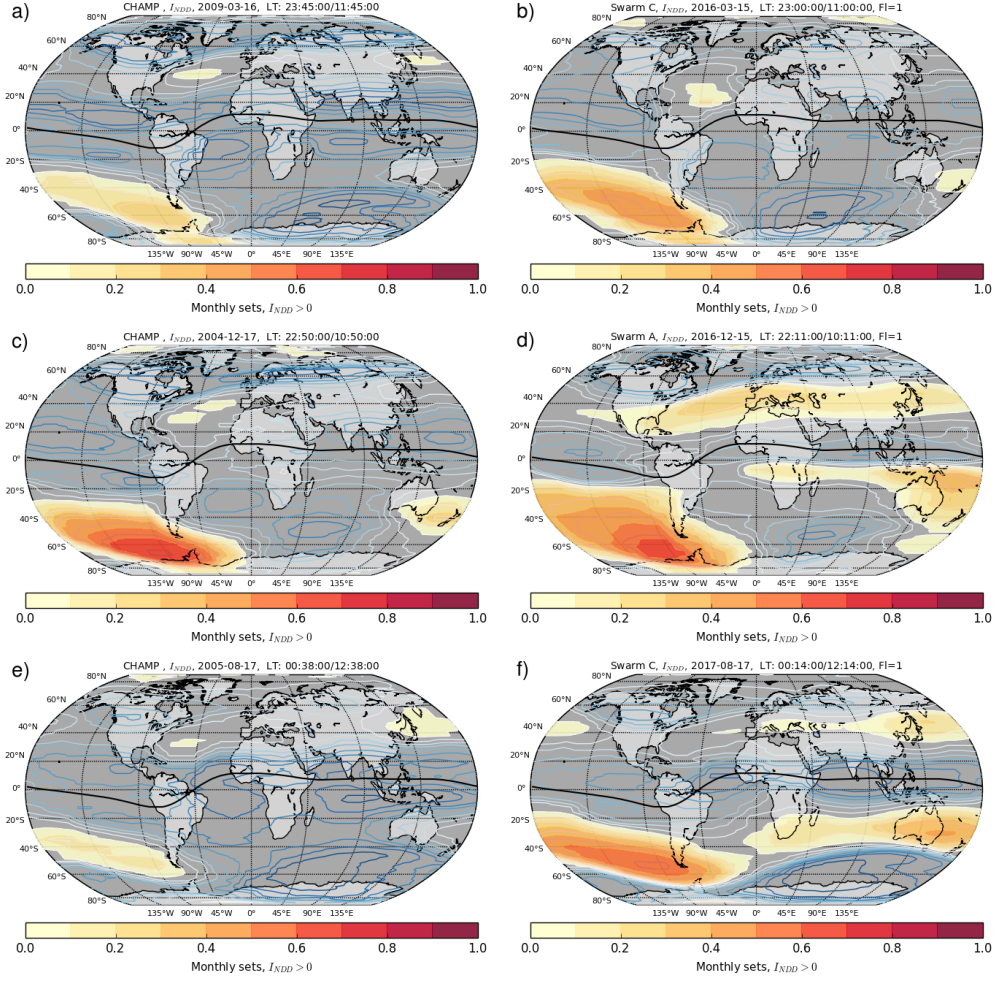


Figure 1. Global maps of I_{NDD} derived from in-situ electron density measured onboard CHAMP and Swarm representing matching LT and seasons. Maps show regions where $I_{NDD} > 0$, indicating global pattern of WSA-like features. Left column presents data from CHAMP (a., c., e.), right column Swarm A/C (b., d., f.).

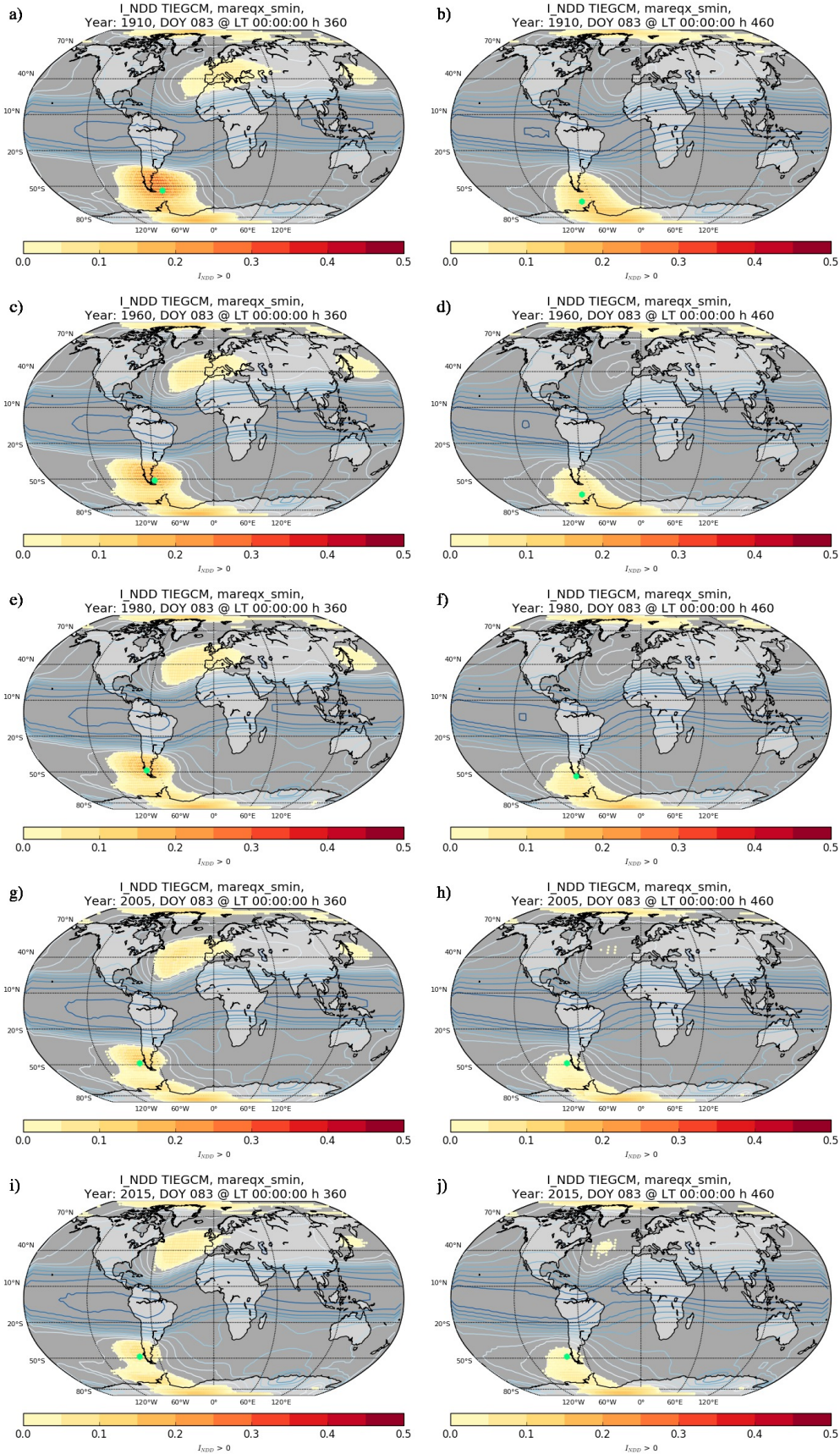


Figure 2. Synthetic index at the altitude of 360 km (left column) and 460 km (right column), for epochs: 1910, 1960, 1980, 2005, 2015. Green point indicates maximum of the index in the region of the WSA.

Table 2. Averaged position of maxima of I_{NDD} for specified LT bin derived from available measurements of Swarm and CHAMP missions

Satellite	LT bin	Long./Lat.
CHAMP	22/10	90°W/ 60°S
Swarm A	22/10	105°W/ 62.5°S
Swarm B	22/10	105°W/ 63.5°S
Swarm C	22/10	105°W/ 62.5°S
CHAMP	00/12	85°W/ 63.5°S
Swarm A	00/12	95°W/ 61.5°S
Swarm B	00/12	95°W/ 54.5°S
Swarm C	00/12	95°W/ 61.5 °S
CHAMP	02/14	75°W/ 57.5°S
Swarm A	02/14	85°W/ 56.°S
Swarm B	02/14	85°W/ 53.5 °S
Swarm C	02/14	85°W/ 56.5°S

Table 3. Maxima of I_{NDD} derived from TIEGCM simulations for selected years, at two altitude levels (360 and 460 km) and LT bins of 22/10 and 00/12

Year	Dipole moment	$Max.I_{NDD}$	Long./Lat.	$Max.I_{NDD}$	Long./Lat.
Alt: 360 km	$10^{22} Am^2$	LT 22/10		LT 00/12	
1910	8.27	0.528	65.0°W 38.75°S	0.337	57.5°W 53.75°S
1960	8.03	0.477	72.5°W 38.75°S	0.274	65.0°W 51.25°S
1980	7.91	0.456	72.5°W 38.75°S	0.245	72.5°W 48.75°S
2005	7.77	0.448	80.0°W 41.25°S	0.189	80.0°W 48.75°S
2015	7.72	0.442	80.0°W 41.25°S	0.151	80.0°W 48.75°S
Alt: 460 km					
1910	8.27	0.443	65.0°W 58.75°S	0.189	72.5°W 63.75°S
1960	8.03	0.349	72.5°W 63.75°S	0.131	72.5°W 63.75°S
1980	7.91	0.315	80.0°W 53.75°S	0.123	72.5°W 53.75°S
2005	7.77	0.277	80.0°W 51.25°S	0.076	80.0°W 48.75°S
2015	7.72	0.275	80.0°W 51.25°S	0.075	80.0°W 48.75°S

Secular variation of the Weddell Sea Anomaly and geomagnetic dipole

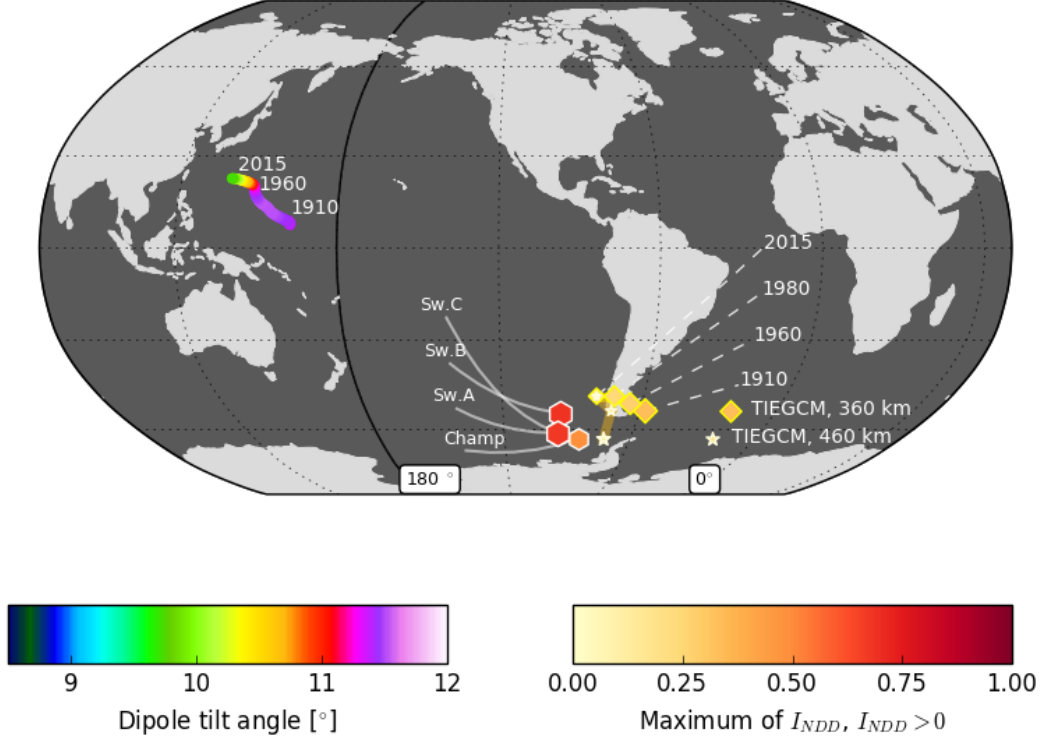


Figure 3. Westward migration of the geomagnetic dipole and the Weddell Sea Anomaly. Rainbow color-palette exhibits reduction of the geomagnetic dipole tilt angle, while the trace marks secular variation of the geomagnetic dipole position projected on the Earth's surface - trajectory derived for time frame 1900 - 2015. Warm toned yellow-red palette applies to maxima of the index I_{NDD} derived from the model (diamond and star markers), and data (hexagonal markers).

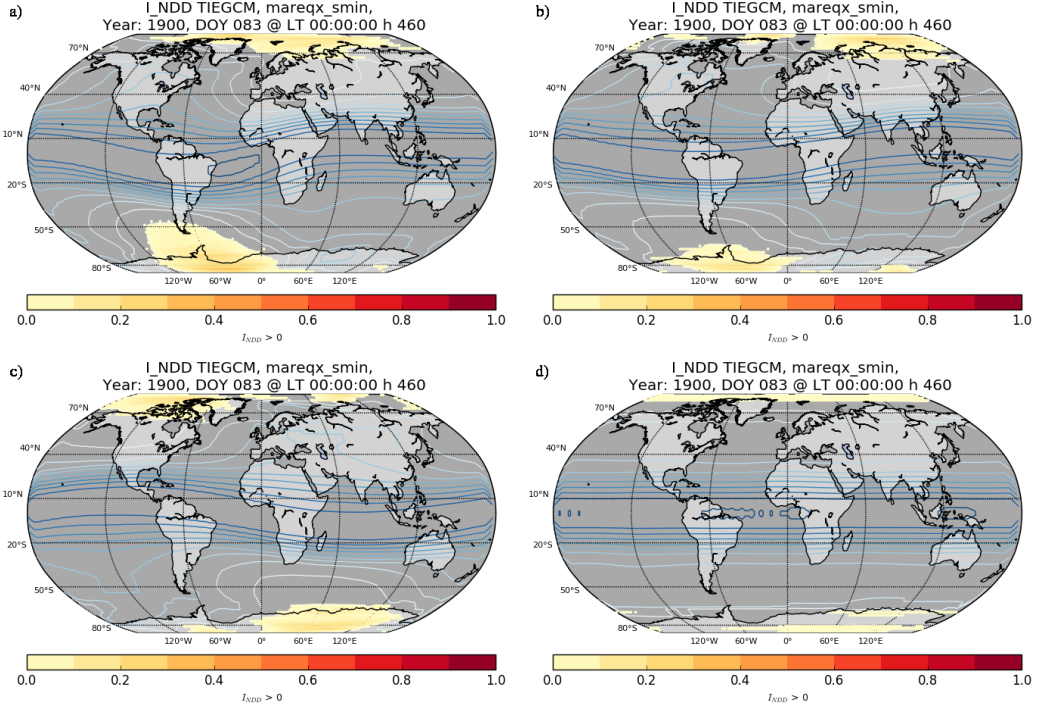


Figure 4. I_{NDD} derived in simplified experiments for LT conditions equal to midnight/noon (LT0000) - a) - tilted eccentric dipole, b) tilted dipole, c) mirrored tilted dipole, d) axial dipole

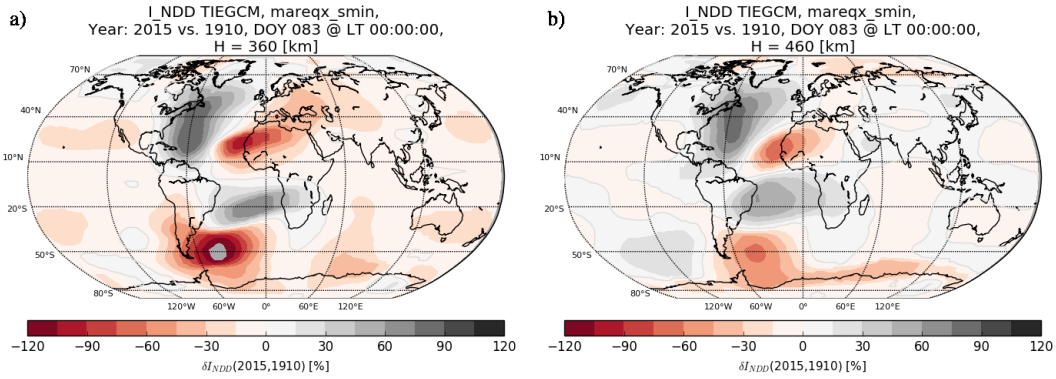


Figure 5. Percentage difference δI_{NDD} of the synthetic index, based on difference between epochs (2015 and 1910). Panel a) represents altitude of 360 km, and b) is for 460 km.